UNIVERSITÀ DI PARMA
ARCHIVIO DELLA RICERCA

University of Parma Research Repository

The adaptation of lipid profile of human fibroblasts to alginate 2D films and 3D printed scaffolds

This is the peer reviewd version of the followng article:

Original
The adaptation of lipid profile of human fibroblasts to alginate 2D films and 3D printed scaffolds / Zanotti, I.; Marando, S.; Remaggi, G.; Bergonzi, C.; Bernini, F.; Bettini, R.; Elviri, L.. - In: BIOCHIMICA ET BIOPHYSICA ACTA-GENERAL SUBJECTS. - ISSN 0304-4165. - 1865:1(2021), p. 129734. [10.1016/j.bbagen.2020.129734]

Availability:
This version is available at: 11381/2881578 since: 2021-12-20T10:36:00Z

Publisher:
Elsevier B.V.

Published
DOI:10.1016/j.bbagen.2020.129734

Terms of use:
openAccess

Anyone can freely access the full text of works made available as "Open Access". Works made available

Publisher copyright

(Article begins on next page)

11 October 2022

The adaptation of lipid profile of human fibroblasts to alginate 2D films and 3D printed scaffolds

Ilaria Zanotti, Silvia Marando, Giulia Remaggi, Carlo Bergonzi, Franco Bernini, Ruggero Bettini, Lisa Elviri*

[1]Department of Food and Drug Science, University of Parma, Parco Area delle Scienze 27/A, 43124, Parma, Italy.

* Corresponding Author: Prof. PhD Lisa Elviri

Phone: +39 0521 905087

Fax: +39 0521 905006

E-mail: lisa.elviri@unipr.it

Highlights

- 2D films and 3D printed scaffolds from alginate
- LC-MS/MS lipid investigation on ALG action mechanism on fibroblasts
- Ceramides modulation after cell-biomaterial interactions

Abstract

Background: The investigation of the interactions between cells and innovative, active material is pivotal in the emerging 3D printing-biomaterial application fields. Here, lipidomics has been used to explore the early impact of alginate (ALG) hydrogel architecture (2D films or 3D printed scaffolds) and the type of gelling agent ($CaCl_2$ or $FeCl_3$) on the lipid profile of human fibroblasts.

Methods: 2D and 3D ALG scaffolds (2D_ and 3D_ALG)were prepared and characterized in terms of water content, swelling, mechanical resistance and morphology through SEM analysis before human fibroblast seeding (8 days). Using a liquid chromatography-triple quadrupole-tandem mass spectrometry approach, selected ceramides (CER), lysophosphatidylcholines (LPC), lysophosphatidic acids (LPA) and free fatty acids (FFA) were analyzed.

Results: The results showed a clear alteration in the CER expression profile depending of both the geometry and the gelling agent used to prepare the hydrogels. As for LPCs, the main parameter affecting their distribution is the scaffold architecture with a significant decrease in the relative expression levels of the species with higher chain length (C20 to C22) for 3D scaffolds compared to 2D films. In the case of FFAs and LPAs, only slight differences were observed as a function of scaffold geometry or gelling agent.

Conclusions: Variations in the cell membrane lipid profile were observed for 3D cell cultures compared to 2D and these data are consistent with activation processes occurring through the mutual interactions between fibroblasts and ALG support. These unknown physiologically relevant changes add insights into the discussion about the relationship between biomaterial and the variations of cell biological functions.

Keywords

Ceramides, fatty acids, lysophosphatidic acids, lysophosphatidylcholines, human fibroblasts, 3D printing, alginate, liquid chromatography-mass spectrometry

1. Introduction

In the recent years the development of innovative active materials in combination with new production technologies (i.e. micro- and nano-systems, 3D printing, electrospinning, etc.) is of growing interest in several research and application fields (i.e. drug delivery, regenerative medicine, gene therapy, *in vitro* diagnostic tests, etc.) [1-3]. The driving idea is to overcome essential limitations of traditional approaches (i.e. introduction of more reliable diagnostic tests, improvement of drug delivery systems, bio-fabrication of tissues or organ-like systems etc.), and many efforts are made to evaluate the effectiveness of these systems through *in vitro* and *in vivo* studies.

In such a context, the investigation of the interactions between cells and biomaterials- is pivotal to obtain a more comprehensive mechanistic understanding of the cause-effect relationships of the whole system. The capability to offer thorough pictures of these complex living processes allow to drive new development strategies in the huge application landscape of biomaterials. However, many challenges still remain open, as it is well known that cell behavior depends upon several factors, including microenvironment dimensions, structure and chemico-physical composition.

Biomaterials interact with the cells at various length scales, from that of individual cells (micrometers) to the that (nanometers) of single molecules (i.e. proteins, lipids). These interactions are based on both physical contact and chemical binding and depend over time as a function of the dimension of the system. Individual cells interact via integrin with a biomaterial for days or weeks, while individual proteins, or lipids or glycosaminoglycans interact through secondary bonds and hydrophobic interactions on time scales as short as seconds and minutes [4, 5]. A complex network of non-covalent kinetically rapid interactions such as hydrogen bonds, van der Waals and hydrophobic interactions can affect the more driving and thermodynamically stable ionic interactions.

104 The spatial architecture, surface area, interstitial pore distribution and dimensions of native
105 extracellular matrix (ECM) strongly influence the cell migration, proliferation and differentiation [6].
106 Biomaterial surfaces can induce changes either in the cell membrane fluidity and permeability, which
107 in turn regulate cellular and tissue functions, or in cell phenotype, including morphology,
108 proliferation and biochemical properties [7, 8]. For example, the surface and inner pore size of a
109 scaffold influence the migration speed of cells: in collagen-GAG scaffolds the smaller is the average
110 pore size, the lower is fibroblast migration speed [9-11]. Nonetheless, it has been shown that prostate
111 cancer cells migrate faster than fibroblasts through the same scaffold [12]. It is clear that the
112 knowledge of these effects at the molecular level can help to develop and tune optimal biomaterials
113 and scaffolds as a function of the application.
114 Alginate (ALG) is a widely investigated biomaterial used in drug delivery and in many biomedical
115 applications thanks to its excellent properties, such as biocompatibility, low toxicity, low cost and
116 ability to undergo spontaneous gelation under mild conditions [13-16]. ALG is a natural occurring
117 anionic polymer extracted from the brown algae cell wall. It is an unbranched binary copolymer
118 consisting of the repetition of the monomer units D-mannuronic acid (M) and L-glucuronic acid (G),
119 held together by β1-4 bonds [17]. During ionotropic gelation a network of interactions involving
120 different junction zones (i.e. -OH, COO^- and $-O^-$ groups) of consecutive G-residues of the ALG chains
121 and the cation occurs. Calcium chloride ($CaCl_2$) represents one of the most used crosslinking agent
122 for the formation of the ALG ionotropic hydrogel. The divalent cations bind only to the glucuronic
123 acid blocks of the ALG chains forming a cross-linking model called "egg-box", resulting in a gel
124 structure. Conversely, chelation with the trivalent Fe^{3+} ions allows for more spherical shapes [18]. In
125 general, the speed of gelation is an important parameter to control the uniformity and shape of the
126 gel. Slower gelation leads to the production of more uniform structures and greater mechanical
127 integrity [19]. Furthermore, better cell adhesion and proliferation have been observed on ALG
128 matrices when the latter is gelled with trivalent ions, such as Fe^{3+} [20].ALG, as cross-linked hydrogel
129 deriving from a natural polysaccharide, presents structure, flexibility, porosity and diffusive transport

130 characteristics similar to the ECM of human native tissues and is used in regenerative medicine as
131 dressings to keep a wound moist, minimize battery infection and accelerate the healing process [18].
132 Among applications ALG is widely exploited for the controlled release of drugs and proteins, for the
133 transport of cells to a specific site [21-23] and to perform two-dimensional (2D) and three
134 dimensional (3D) cell studies to understand cell-matrix interactions.
135 Although cells in a living system are exposed to complex 3D biological environments, biological
136 phenomena is still extensively investigated by means of 2D substrates. 2D assays present major
137 limitations to accurately describe the space constraints of cells *in vivo* and can induce different cell
138 activities and/or loss of the original cell phenotype. 2D films are still widely used in several cell
139 culture experiments, but 3D printing manufacturing process is rapidly gaining a prominent role as
140 innovative technology in the medical or diagnostic fields to shape biopolymers in a variety of
141 architectures to progressively replace two dimensional systems [24-29].
142 With the aim to improve the basic knowledge available in the cell-biomaterial interaction field, in
143 this study the effects of different architectures and gelling media used for the preparation of ALG
144 hydrogels were investigated for the first time on the targeted lipid profile of human fibroblasts.
145 Controlled and reproducible 2D films (2D-ALG) and 3D printed ALG scaffolds (3D-ALG) were
146 produced by gelation with $CaCl_2$ or iron chloride ($FeCl_3$), and a selected targeted lipid profile of
147 human fibroblasts seeded on them was evaluated. Cell biochemistry can be studied at different
148 complementary levels (i.e. the transcriptome, proteome, lipidome or metabolome) to gain information
149 useful to frame their behavior [30, 31]. Here we decide to focus our attention on lipids, as they play
150 a crucial role in the physiology of cells, tissues and organs as demonstrated by a large number of
151 genetic studies [32]. The deregulation of lipid metabolic pathways therefore leads to the onset of
152 diseases, including cardiovascular disorders, cancer and diabetes [33-35].
153 Lipidomics is nowadays a consolidated field capable of a comprehensive analysis of lipids in complex
154 biological systems. Lipidomics aims to profile the lipid structures and quantity in a biological sample,
155 to assess their metabolic functions and transformations that occur in different physiological and

156 pathological conditions [36]. The birth of lipidomics has been possible thanks to technological
157 advances in the field of analytical instrumentation such as mass spectrometry (MS) [37-39]. This set
158 of techniques is the golden standard approach for the investigation of the lipids in cells by virtue of
159 their ability to perform the simultaneous identification and quantification of thousands of analytes in
160 the same biological sample. Here a liquid chromatography-electrospray-tandem mass spectrometer,
161 with a triple quadrupole mass analyzer, was used for the identification and relative quantitative
162 detection of lipids belonging to the following classes, selected as powerful mediators of cell
163 functions: ceramides (CER), fatty acids (FFA), lysophosphatidic acids (LPA) and
164 lysophosphatidylcholines (LPC). CER and FFA are lipid species that modulate membrane rigidity,
165 creating micro-domains, and altering membrane permeability, thus regulating cell membrane
166 functions [40]. Moreover, CER enhance the bioavailability of drugs by acting as lipid delivery
167 systems, they play a structural role in liposome formulations and enhance the cellular uptake of
168 amphiphilic drugs, such as chemotherapics [41]. In a recent study FFA have been chemically linked
169 with biological drug molecules to enhance oral absorption of therapeutic peptides and to provide a
170 platform for oral peptide drug development [42]. LPA derivatives are bioactive phospholipids present
171 in biological fluids that regulate many important fibroblast functions, including proliferation,
172 migration and contraction. Alteration in normal LPA signaling may contribute to a range of diseases,
173 including neurodevelopmental and neuropsychiatric disorders, pain, cardiovascular disease, bone
174 disorders, fibrosis, cancer, infertility, and obesity [43]. Therefore, therapies targeting LPA
175 biosynthesis and signalling may be feasible for the treatment of devastating human diseases [44].
176 LPC are present as minor phospholipids in the cell membrane and blood plasma, promote
177 inflammatory effects [45] and play a role in the pathway of fibrotic injury in human cardiac fibroblasts
178 [46].
179

180 ## 2. Materials and methods

181 ### 2.1. Reagents

Acetonitrile, methanol, hexane and isopropanol were supplied from Sigma-Aldrich (Taufkirchen, Germany). Water was purified (0.055 uS/cm, TOC 1ppb) with a Purelab pulse + Flex ultra-pure water system (Elga Veolia, Milan, Italy).

2.2. Scaffold preparation

ALG formulation (Ph.Eur. grade; molecular weight by gel filtration chromatography (GFC) 180–300 kDa; slowly soluble in water, Carlo Erba, Italy) was prepared by dissolving the sodium ALG 6% (w/v) in deionized water. The formulation was left under stirring overnight on a magnetic plate until a homogeneous mixture was obtained. The ALG films (2D scaffolds) were obtained by pouring the 6% ALG formulation onto a glass plate and then stretching it using a 0.6mm film-stretcher. The two casting solutions were left to dry in an oven at 40 °C for minutes and 2 and a half hours, respectively. At this point, the dried alginate films were immersed in the solutions of $CaCl_2$ 3% (w/v), (anhydrous $CaCl_2$, lot. 419887/1, Fluka Chemie GmbH, Switzerland) or $FeCl_3$ 3% (w/v), (anhydrous $FeCl_3$ 98%, lot. H29Y005, Alfa Aesar, United States) to cross-link for one hour. Subsequently, films were detached from the glass plates and rinsed twice in deionized water for 15 min.

The 3D ALG scaffolds were made by using a 3D printer built in house (38). The machine is based on a three cartesian axes system that allows the movement on the horizontal plane of printing plate and the vertical translation of the nozzle. ALG solution was loaded into a 10 ml syringe and was extruded by a pump acting on a syringe mounting a 26G needle, deposed, layer by layer, on the printing plate at a velocity of 3 mm/s and instantaneously frozen (-14 °C) with a series of Peltier cells which allows the material, to freeze instantly and maintain the three-dimensional structure. At the end of the print, the steel plate with the scaffold is removed and immersed in the gelling solution ($CaCl_2$ 3% (w/v) or $FeCl_3$ 3% (w/v)) for one hour. At the end of the gelling process, the scaffold is rinsed in deionized water to remove all traces of the gelling agent.

2.3. Evaluation of water content

To determine the water content, 3D (5-layer square with a side of 1.4 cm) and 2D (2mm-thick) ALG scaffolds gelled in $CaCl_2$ (ALG_Ca) or in $FeCl_3$ (ALG_Fe) were prepared. After being molded, the scaffolds were gelled for 1 hour in the respective gelling agents and subsequently rinsed in deionized water. The scaffolds were lightly buffered on absorbent paper and weighed on an analytical balance to determine the wet weight (Ww). Subsequently, the scaffolds were dried in an oven at 40 °C overnight and weighed again to determine their dry weight (Wd). Five replicates were analyzed. The water content (Wc) was calculated as:

$$WC = \frac{(Ww - Wd)}{Ww * 100}$$

2.4. Swelling test

The swelling behavior of the scaffolds was evaluated over time (1 min, 30 min, 1h, 2h, 6h, 24 hours) by measuring their weight. To perform the test, 5-layer square ALG scaffolds were created, with a side of 1.4 cm. After printing, the scaffolds were gelled for 1 hour in the respective gelling agents and subsequently rinsed in deionized water and dried in an oven at 40 °C overnight before weight measurement. Subsequently, each scaffold was placed in deionized water and the weights were taken at each time interval. Before each measurement, the scaffolds were swabbed on absorbent paper to eliminate surface drops. Five replicates were analyzed. The swelling ratio (Qs), defined as the average percentage of swelling, was assessed through the following equation:

$$Qs = \frac{(Ws - Wd)}{Wd}$$

where Ws represents the weight of the scaffold at a certain time and Wd is its initial weight.

2.5. Mechanical properties

The mechanical resistance of ALG_Ca or ALG_Fe was measured by using 3D 20-layers scaffolds and 2mm-thick ALG films having size of 5 cm x 1.5 cm. Thickness was determined (n. of replicates = 6) with a digital micrometer (Mitutoyo, Japan). Each scaffold was fixed on a tensile tester (AG M1

Acquati, Italy) loaded with a 5 daN cell. Force and time signals were digitalized by means of a PowerLab 400 board and recorded with the Scope v.3.5 software. Elongation at break (% strain) and Young's modulus were determined from the relevant stress-strain curves, taking into consideration the linear portion. Three replicates were analyzed.

2.6. SEM analysis

SEM analysis were carried out to study the morphology and pore distribution of 2D_ALG and 3D_ALG . 2D_ALG (n=3) or 3D_ALG 10-layers square (1.5x1.5 cm)gelled in $CaCl_2$ or in $FeCl_3$ were prepared . The samples were immersed in increasing concentrations of ethanol (10%, 20%, 30%, 40%, v/v in dH_2O) 10 minutes for each step. Subsequently, the samples were subjected to freeze-drying for 24 hours in the Christ Alpha 2-4 LSC plus Freeze Dryer and gold sputtered through a metallizer (Balzers). Surface and section images of 3D samples were captured at different magnifications, ranging from 80X to 640X. Photographs of 2D film surfaces were acquired at 300X magnification. For the acquisition of the images of 2D_ALG a scanning electron microscope (Sigma HD, Carl Zeiss, Jena, Germany) at EHT 1.00 kV was used while a SEM 501 (Philips) was employed for 3D scaffold characterization. All images were analyzed by ImageJ software (NIH, Bethesda USA) for the measurement of macro- and micro-structures, mean pore size (Feret diameter) and distribution.

2.7. Cell culture

Primary human skin fibroblasts, coded as C86, were derived from a forearm biopsy of a healthy donor after signature of an informed consent. Cells were maintained in Dulbecco's Modified Eagle's Medium (DMEM, Gibco) culture medium, supplemented with 1% (v/v) of L-glutamine (Gibco), 1% of Streptomycin and Penicillin (Gibco), 1% of Na-pyruvate (Gibco), 1% of NEAA (Non-Essential AminoAcids, Gibco) and 10% of FBS (Fetal Serum Bovine, Euroclone). After overnight disinfection in ethanol 70 % (v/v in dH_2O), 2D_ALG and 3D_ALG were deposited in 12-well plates (Constar)

and washed with sterile water. The following conditions have been tested: positive control (represented by the seeding of cells directly in the well); 2D_ALG_Ca; 3D_ALG_Ca ; 2D_ALG_Fe; 3D_ALG_Fe ; negative control (represented by films and scaffolds without cells).

500k cells per well were seeded (150 µl) directly on 2D and 3D scaffolds to observe the impact of microenvironment on cell behavior and 850 µl of 10% FCS medium were added to reach the volume of 1 ml. Cells were incubated and maintained for 8 days at 37° C, 5% CO_2 (Incubator Nabco, Chicago, IL, USA).

2.8. MTT assay

The MTT assay was carried out as follows: 500 µl of a solution consisting of MTT (1 mg/ml) and 5% FCS medium were added to each well. The cells were incubated for 2h at 37 °C. After two hours, the MTT and medium solution was aspirated and the films and scaffolds were transferred into new plates. 500µl of DMSO (dimethylsulfoxide) were added to each well and the plates were stirred on a tilting plate for 15-20 minutes at room temperature. From each well 200µl were taken and placed in a 96-well plate (Constar, Flat Transparent) for spectrophotometric reading. Each sample was analyzed in duplicated. 200µl of DMSO was added to two wells of the plate to be used as a control. Spectrophotometry reading was carried out at a wavelength of 570 nm. The spectrophotometer used is a TECAN Spark 10M spectrophotometer. The data relating to the analysis were processed by subtracting the absorbances obtained from the cell-free supports (negative controls).

2.9. Lipid extraction

The extraction of lipids from cellular matrices was performed by using a mixture of hexane and isopropanol (3:2; v/v). Cells grown on plastic and ALG films were detached using trypsin, centrifuged and resuspended in iced sterile water. To detach the cells grown on the 3D scaffolds an EDTA-Na citrate (EDTA 50 mM; Na citrate 55 mM) solution was used to dissolve the scaffolds. The contents of the wells were centrifuged and the pellet was resuspended in iced sterile water. The cell suspension

obtained was transferred to cryotubes and cell lysis was obtained by 2 freezing cycles in liquid nitrogen and thawing at 37 ° C for 10 minutes. Subsequently, the samples were transferred into glass tubes and 360 µl of hexane and 240 µl of isopropanol were added. After being vortexed for 1 min, the tubes were centrifuged (2000 rpm x 5 min). The organic phase was transferred to new glass tubes, and the procedure was repeated twice. The supernatants obtained were evaporated under nitrogen stream and resuspended in 50 µL of methanol before LC-MS analysis.

2.10. Liquid chromatography-mass spectrometry analysis

The analyses were carried out by using an HP1200 Agilent LC system (Agilent Technologies, USA) equipped with an electrospray QTRAP 4000 mass spectrometer (ABSCIEX, CA, USA). The chromatographic separation was carried out on C18 (50x2.1 mm, 5 µm) column (Phenomenex, CA, USA). Mobile phase was (A) methanol and (B) acetonitrile. The mobile phase was filtered through a 0.45 µm cellulose membrane before use. Flow-rate was 0.2 mL/min and the injected volume was 10 µL. The system was controlled by the Analyst software v. 1.4. (ABSCIEX). Source parameters were: negative ion (NI) ESI voltage, -4.5 kV; declustering potential, -50 V; entrance potential, -10V; source temperature, 350 °C and positive ion (PI) ESI voltage, 5.5 kV; declustering potential, 50 V; entrance potential, 10V; source temperature, 350 °C. Quadrupoles were tuned to unit resolution. As for quantitative analysis, experiments were performed under PI- or NI-SRM conditions using nitrogen as collision gas (medium nitrogen pressure). The SRM transition considered in this study are reported in the Table 1 of the supplementary material. The analytes were relatively quantified among samples and normalized for MTT assay. The chromatograms were analyzed through the MultiQuant software (version 2.1).

2.11 Statistical analysis

Comparisons between groups were made by one-way ANOVA with Tukey's correction for multiple testing. The data from LC/MS analysis have been expressed as % of the individual lipid specie on the

total amount of lipids on each biomaterial. Given the large number of observations that are highly correlated with each other, no statistical analysis was made for comparison of lipid species profiles within the four biomaterials.

3. Results and discussion

3.1. 2D_ALGand 3D_ALG preparation and characterization

In the first part of the work the preparation and characterization of the 2D_ALG and 3D_ALG (Figure 1) were addressed in order to study the effects of the different gelling media on the final hydrogel properties. In general, ALG presents different chelating affinity for its cross-linking cations, as a function of their charge and dimensions, resulting in hydrogels having different properties such as swelling, elasticity and stability.

The determination of the water content, a parameter that allows to evaluate the ability of the scaffolds to absorb biological fluids and keep the tissues hydrated, displayed that both 2D_ and 3D_ALG_Fe retain very similar percentage of water (93±1%) compared to 2D_ and 3D_ALG_Ca (90.1±0.8%).

The swelling tests showed that, in general, ALG_ Ca immersed in deionized water tend to swell up to 6h. ALG_Fe, on the other hand, showed this behavior only up to 2h (Figure 2). The ALG scaffolds were also submitted to stress-strain tests. The maximum stress (MPa) was calculated by dividing the force applied at the breaking point (N) by the cross section area of the specimens (mm^2). Another test used was the tensile test that allowed to determine Young's modulus, (modulus of elasticity). The viscoelastic behavior of the scaffolds was therefore determined.

3D_ALG_Cashowed greater mechanical strength (5.7±1.1 N) and therefore required greater strength to be broken, while 3D_ALG_Fe scaffolds were less resistant (4.9±1.0 N). 3D_ALG_Ca scaffolds were characterized by greater elasticity (6.5 ± 0.4 MPa), than 3D_ALG_Fe, which were extremely rigid (0.72 ± 0.05 MPa). The gelling agent, therefore, caused a change in the elastic behavior of the

334 ALG, making it particularly elastic and resistant when gelled with $CaCl_2$ and excessively rigid and
335 less resistant when crosslinked with $FeCl_3$.
336 2D_ALG were also characterized for their mechanical behavior. As for 3D_ALG, a macroscopic
337 difference in terms of consistence was noticed between samples gelled by the two media. In particular,
338 2D_ALG_Ca appeared stiff but much less rigid compared to 2D_ALG_Fe .
339 Measurements showed an average Young's modulus of 3.3 ± 1.5 MPa and 26 ± 8 MPa for
340 2D_ALG_Ca and 2D_ALG_Fe, respectively. 2D_ALG_Ca showed an elastic behavior only during
341 the first phase of longitudinal traction, followed by deformation of the samples (plastic behavior) and
342 consequent rupture. 2D_ALG_Fe showed instead a linear increase of stress over strain until breakage,
343 that occurred very early due to the rigidity of the tested material.
344 The higher elasticity and plasticity of 2D_ALG_Ca was demonstrated as well by the calculation of
345 percent elongation, whose mean value resulted 20.3 ± 9.9 %. In comparison, 2D_ALG_Fe showed a
346 significantly lower strain, with a maximum percent elongation of 3.0 ± 1.5 %. While 2D_ALG_Ca
347 highlighted suitable features for potential adoption as material for regenerative medicine,
348 2D_ALG_Fe demonstrated overall weak mechanical properties, being very rigid, devoid of elasticity
349 and capability to flex or strain without breakage.
350 As for morphological characterization, SEM analysis was carried out to evaluate the microstructure
351 of the ALG scaffolds. The scaffolds should have a high porosity and an interconnected pore structure
352 suitable for penetration, as well as adhesion, proliferation and cell differentiation. Figure 3 displays
353 the pore size distribution, on surface of 3D_ALG_Ca scaffolds **(Figure 3a-b)** and of 3D_ALG_Fe
354 (Figure 3d-e). In the first case the average pore size, expressed as Feret's diameter, was between 11-
355 45 μm; while in the second case the average pore size was higher (between 11-126 μm). This
356 difference could be attributed to the gelling agent which leads to the formation of more or less large
357 pores during the gelation process of the biomaterial. In both cases, the pore size was adequate for the
358 penetration of fibroblasts which had a diameter ranging from 15 to 20 microns.

The longitudinal cross-section of 3D_ALG_Ca exhibited high porosity with homogenous distribution (5-40 μm) (Figure 3c). 3D_ALG_Fe showed regular tubular morphology mimicking a vessel-like structure (Figure 3f), where the inner diameters of the hollow filaments range from 50 μm to 140 μm. This morphological behavior strongly depends on the gelling conditions and can be useful to design scaffolds with tunable shapes for further applications in regenerative medicine or drug delivery. The differences observed between the effects of the two gelling media can correlate with the differences between the mechanical properties described above. In fact the 3D_ALG_Ca showed greater mechanical strength, compared to theless resistant 3D_ALG_Fe.

2D_ALG present much less porous compared to 3D_ALG. Few pores having dimensions of 10 to 20 microns are randomly spread on the surfaces of overall compact structures. 2D_ALG_Fe (Figure 3h) showed the presence of cracks in the polymeric structure, intermitted by rougher and more corrugated surfaces compared to 2D_ALG_Ca (Figure 3g).

3.2. LC-MS/MS SRM analysis of the fibroblast lipid profile

The expression of CER, LPC, LPA and FFA was evaluated to understand how and if the geometry of 2D_ and 3D_ALG or the gelling agents are able to affect their relative expression levels in dermal human fibroblasts.

Before LC-MS/MS analysis, the viability of the cells in contact with the 2D_ and 3D_ALG was quantitatively assessed after 8 days by MTT colorimetric assay. Biocompatibility was demonstrated for 2D_ and 3D_ALG_Ca (approx. 70% vs cells grown on Petri dish), and for 2D_ and 3D_ALG_Fe (approx. 26 % vs cells grown on Petri dish) (Figure 4). In this latter case,a lower vitality percentage was obtained, but it should be noted that these supports were more difficult to handle because of a reduced structural stability in the cell culture media. It was observed that the cell culture medium impacted on the scaffold structure. In particular, ALG_Fe tended to dissolve in the medium over the experimental time (images not shown), whereas ALG-Ca retained their structure. Such results could

384 be in agreement with the different mechanical properties of the hydrogels obtained with calcium and
385 iron or even with the affinity of the substances present in the culture medium toward the cations.

386

387 **3.3. Ceramides**

388 Nineteen CER d18:1 containing species were determined by targeted MS analysis. Among them, a
389 remarkable variability was observed as a function of the scaffold preparation. The results obtained
390 clearly show that the relative expression of these lipids was significantly affected by both the structure
391 of the scaffolds and the gelling agents employed (Figure 5).
392 The most abundant species, represented by CER d18:1-16:0 and CER d18:1-22:0, showed a peculiar
393 expression in response to the structure and the composition of the supports. The former reveals
394 significantly higher amount on 2D_ALG_Ca than on 2D_ALG_Fe and on 3D_ALG_Ca, while the
395 opposite was observed in the latter. In addition, CER d18:1-22:0 was more abundant when cells were
396 grown on 2D_ALG_Fe compared to 3D_ALG_Fe. In the relatively less expressed species, a well-
397 defined trend is evident: the short chain ceramides (CER d18:1-16:1, CER d18:1-20:0) present higher
398 expression on the 2D_ALG_Ca compared to 3D_ALG_Ca, while the opposite occurs for long chain
399 ceramides (CER d18:1-22:2, CER d18:1-22:5). The influence of the support composition is evident
400 for many lipid species, that presented higher abundance on 2D_ALG_Ca(CER d18:1-16:0, CER
401 d18:1-16:1, CER d18:1-20:0, CER d18:1-22:0, CER d18:1-22:2, CER d18:1-22:5) or 3D_ALG_Ca
402 (CER d18:1-22:0, CER d18:1-22:2, CER d18:1-22:5) compared to the respective support made with
403 $FeCl_3$. These findings suggest that, although the biomaterial and the geometry are the same, its surface
404 morphology and the presence of Ca^{2+} or Fe^{3+} ions could significantly increase the production and the
405 quali- and quantitative distribution of this class of compounds.
406 In addition, LC-MS/MS chromatograms revealed that ceramides exist as a balance mixture of two
407 isomers (data not shown). In particular, two isomeric forms were observed for CER d18:1-16:0, CER

d18:1-20:0, CER d18:1-22:0, CER d18:1-22:1, CER d18:1-22:2, with one isomer predominating over the second isomer, regardless of the architecture of the scaffold and the gelling agent.

3.4. LPC

The most representative LPC monitored were 16:0, 18:0 and 18:1 in all samples, whereas the other species were present in much lower amount (Figure 6). LPC 16:0, LPC 18:0 and LPC 18:1 show a very similar relative expression level in all the tested conditions. On the other hand, many minor components of this class reveal significantly higher abundance when cells were grown on 2D_ALG than on 3D_ALG. This is the case for LPC 20:2, LPC 20:3, LPC 20:4, LPC 22:4, LPC 22:5 and LPC 22:6, when the gelling agent was $FeCl_3$, and for LPC 20:2, LPC 22:5 and LPC 22:6 when $CaCl_2$ was employed. Interestingly, the influence of the gelling agent was observed for LPC 18:2, LPC 20:4 and LPC 22:0, where higher abundance was observed in 3D_ALG_Ca than in 3D_ALG_Fe.

All together these findings suggest that, although the main LPC composition is maintained, both the gelling agent and the scaffold structure may somehowaffect LPC distribution .

As previously, LPC were detected as two isomeric forms, but no significant differences were observed in terms of relative intensities between the two gelling media or scaffold geometries.

3.5. LPA

LPA are usually present at very low concentrations in cell membranes and their detection is challenging. Using the LC-MS/MS method here proposed, the most abundant lipid detected was the 16:0 specie in all samples (Figure 7). The data collected for LPA showed that the relative trend of these lipids was generally maintained with some slight differences especially related to the geometry of the scaffold. A significant increase of abundance in 2D_ALG_Fe vs 3D_ALG_Fe was observed for LPA 17:0 and LPA 20:1, while statistical difference was not reached for LPA 22:0. Consistently, a trend towards increased expression on 2D_ALG_Ca and 2D_ALG_Fe compared to respective 3D_ALG was observed for LPA 18:0. The abundance of this lipid specie was also influenced by the

gelling agent, since an increase of expression in 2D_ and 3D_ALG_Ca versus 2D_ and 3D_ALG_Fe was observed, despite not statistically significant.

3.6. FFA

Among the detected FFA, the most abundant species were 20:0 and 22:0. No significant differences were observed in the general trend of FFA on the different supports (Figure 8). Only an increase in the expression level of two minor species (FA 20:4 and FA 22:1) was observed when cells were grown on 2D_ALG_Ca vs 3D_ALG_Ca. These data suggest that FFA are not susceptible of significant influence neither from the geometry nor from the gelling agent .

4. Conclusions

3D cell cultures can add unknown physiologically relevant aspects compared to 2D.

Here the behavior of fibroblasts as well as their lipid profile in contact with ALG systems was demonstrated to be influenced both by the architecture (2D or 3D) and the type of gelling agent . 2D_ and 3D_ALG were prepared by using two gelling agents ($CaCl_2$ or $FeCl_3$), and characterized from a chemical-physical point of view through determination of the water content, swelling tests and mechanical resistance tests and from a morphological point of view through SEM analysis. The water content determination has shown that ALG_Fe had a slightly higher water content than ALG_ Ca , i.e. 92% and 90% respectively. The mechanical resistance tests have shown that the ALG_Ca had a greater elasticity than ALG_ Fe, which were extremely rigid. Thus, the former needed more strength to break. The swelling tests carried out showed that ALG- Ca swell and expand up to 6h. On the other hand, ALG_Fe, showed this behavior only up to 2h. Finally, the average pore size of scaffolds gelled with both solutions, was suitable for fibroblast (diameter ranging from 15 to 20 microns) adhesion and growth.

A LC-MS/MS targeted approach was exploited to investigate the effects of cell-biomaterial interaction on the profile of selected lipids belonging to CER, LPC, LPA and FFA classes. The results

clearly indicate that significant differences exist in the distribution of CER species in the fibroblasts and that these differences are determined by activation through biomaterial interactions. LPC distribution exhibited some differences among samples, whereas LPA and FFA resulted in more constant trends.

Generally, cell-biomaterial engineered substrate interactions is strongly influenced by mechanical factors and cell membranes exhibit very different behaviors depending on the elasticity of the substrate microenvironment they are anchored. In the case of CER, as abundant bioactive signaling lipids present in the cell membrane, both the architecture and the gelling media affected the relative distribution of these species, playing a fundamental role in the organization of specific membrane regions. In the case of LPC, present as minor phospholipids in the cell membrane, our data suggests that the main parameter affecting their cell membrane lipid distribution is the scaffold architecture with a significant decrease in the relative expression levels of the species with higher chain length (C20 to C22) for 3D_ALG compared to 2D_ALG.

As a final conclusion, different ALG scaffolds have the capabilities to affect the relative distribution profile of the main cell membrane lipids and this aspect could result in changes in the cell membrane properties and in a variation of the cell biological functions (e.g. signaling).

Acknowledgements

The Authors thank Dr. Ivana Lavota, Dr. Giorgia D'Andrea and Mr. Davide Dallatana for the excellent technical assistance.

References

[1] N. Huebsch, D.J. Mooney, 2009. Inspiration and application in the evolution of biomaterials, Nature. 462 (2009) 426–432. https://doi.org/10.1038/nature08601.

[2] M. Mabrouk, H. Beherei, D. Das, Recent progress in the fabrication techniques of 3D scaffolds for tissue engineering, Materials Science and Engineering:C. 110 (2020) 110716. https://doi.org/10.1016/j.msec.2020.110716.

[3] P. Grabiec, 2012. Micro-and Nano-systems for Chemical/Bio-medical Analysis and Diagnostics. Procedia Engineering. 47 (2012) 1502-1505. https://doi.org/10.1016/j.proeng.2012.09.437.

[4] Xiao Zhang, Cui Song, Guanghui Ma, Wei Wei, Mechanical determination of particle–cell interactions and the associated biomedical applications, J. Mater. Chem. B. 6 (2018) 7129-7143. https://doi.org/10.1039/C8TB01590B.

[5] J.A. Sanz-Herrera, E. Reina-Romo, Cell-biomaterial mechanical interaction in the framework of tissue engineering: insights, computational modeling and perspectives, International journal of molecular sciences.12 (2011) 8217–8244. https://doi.org/10.3390/ijms12118217.

[6] S.F. Badylak, D.O. Freytes, T.W. Gilbert, Extracellular matrix as a biological scaffold material: Structure and function, Acta Biomaterialia. 5 (2009) 1–13. https://doi.org/10.1016/j.actbio.2008.09.013.

[7] P. Noutsi, E. Gratton, S. Chaieb, 2016. Assessment of Membrane Fluidity Fluctuations during Cellular Development Reveals Time and Cell Type Specificity. PloS one. 11(6),e0158313. https://doi.org/10.1371/journal.pone.0158313.

[8] N. Mitrousis, A. Fokina, M.S. Shoichet, Biomaterials for cell transplantation, Nat. Rev. Mater. 3 (2018) 441–456. https://doi.org/10.1038/s41578-018-0057-0.

[9] F. O'Brien, B. Harley, I. Yannas, L. Gibson, The effect of pore size on cell adhesion in collagen-GAG scaffolds, Biomaterials.26 (2005) 433-441. DOI: 10.1016/j.biomaterials.2004.02.052.

[10] I.V. Yannas, D.S. Tzeranis, B.A. Harley, P.T. So, Biologically active collagen-based scaffolds: advances in processing and characterization, Philosophical transactions. Series A, Mathematical, physical, and engineering sciences. 368 (2010) 2123–2139. https://doi.org/10.1098/rsta.2010.0015.

[11] J.C. Ashworth, M. Mehr, P.G. Buxton, S.M. Best, R.E. Cameron, Optimising collagen scaffold architecture for enhanced periodontal ligament fibroblast migration, Journal of materials science. Materials in medicine. 29 (2018) 166. https://doi.org/10.1007/s10856-018-6175-9.

[12] K. Miyazaki, J. Oyanagi, D. Hoshino, S. Togo, H. Kumagai, Y. Miyagi, Cancer cell migration on elongate protrusions of fibroblasts in collagen matrix, Scientific reports. 9 (2019) 292. https://doi.org/10.1038/s41598-018-36646-z.

[13] B.A. Aderibigbe, B. Buyana, Alginate in Wound Dressings, Pharmaceutics. 10 (2018) 42. https://doi.org/10.3390/pharmaceutics10020042.

[14] S.H. Aswathy, U. Narendrakumar, I. Manjubala, 2020. Commercial hydrogels for biomedical applications, Heliyon.6(4),e03719. https://doi.org/10.1016/j.heliyon.2020.e03719.

[15] F. Abasalizadeh, S.V. Moghaddam, E. Alizadeh, E. Akbari, E. Kashani, S. Fazljou, M. Torbati, A. Akbarzadeh, Alginate-based hydrogels as drug delivery vehicles in cancer treatment and their applications in wound dressing and 3D bioprinting, Journal of biological engineering. 14 (2020) 8. https://doi.org/10.1186/s13036-020-0227-7.

[16] W.R. Gombotz, S. Wee, Protein release from alginate matrices, Advanced Drug Delivery Reviews. 31 (1998) 267–85. https://doi.org/10.1016/S0169-409X(97)00124-5.

[17] A.D. Augst, H.J. Kong, D.J. Mooney, Alginate Hydrogels as Biomaterials, Macromolecular Bioscience. 6 (2006) 623–633. https://doi.org/10.1002/mabi.200600069.

[18] K.Y. Lee, D.J. Mooney, Alginate: Properties and biomedical applications, Progress in Polymer Science. 37 (2012) 106–126. DOI: 10.1016/j.progpolymsci.2011.06.003.

[19] C.K. Kuo, P.X. Ma, Ionically crosslinked alginate hydrogels as scaffolds for tissue engineering: Part 1. Structure, gelation rate and mechanical properties, Biomaterials.22 (2001) 511–521. DOI: 10.1016/s0142-9612(00)00201-5.

[20] I. Machida-Sano, Y. Matsuda, H. Namiki, *In vitro* adhesion of human dermal fibroblasts on iron cross-linked alginate films, Biomedical materials.4 (2009) 025008. DOI: 10.1088/1748-6041/4/2/025008.

534 [21] K.Y. Lee, D.J. Mooney, Hydrogels for Tissue Engineering, *Chem. Rev.*101 (2001) 1869–1880.
535 https://doi.org/10.1021/cr000108x.
536 [22] J. Bhasarkar, D. Bal, Kinetic investigation of a controlled drug delivery system based on alginate
537 scaffold with embedded voids, Journal of Applied Biomaterials & Functional Materials. (2019).
538 https://doi.org/10.1177/2280800018817462.
539 [23] A. Jagadeesh, G.G. Chaudhari, D.K. Bal, S. Patra, S. Ganguly, Enhancement of Solute Release
540 From Chitosan Scaffold With Embedded Submillimeter Voids, International Journal of Polymeric
541 Materials and Polymeric Biomaterials. 64 (2015) 134-139.
542 [24] M. Saccani, L. Parisi, C. Bergonzi, A. Bianchera, C. Galli, G.M. Macaluso, R. Bettini, L. Elviri,
543 Surface modification of chitosan films with fibronectin fragment-DNA aptamer complex to enhance
544 osteoblastic cell activity: A mass spectrometry approach probing evidence on protein behavior, Rapid
545 Commun Mass Spectrom. 33 (2019) 336-342. https://doi.org/10.1002/rcm.8335.
546 [25] L. Bergamonti, C. Bergonzi, C. Graiff, P. Lottici, R. Bettini, L. Elviri, 3D printed chitosan
547 scaffolds: A new TiO2 support for the photocatalytic degradation of amoxicillin in water, Water Res.
548 163 (2019) 114841.
549 [26] C.Y. Chen, C.J. Ke, K.C. Yen, H.C. Hsieh, J.S. Sun, F.H. Lin, 3D porous calcium-alginate
550 scaffolds cell culture system improved human osteoblast cell clusters for cell therapy, Theranostics.
551 5(2015) 643–655. https://doi.org/10.7150/thno.11372.
552 [27] C. Bergonzi, A. Di Natale, F. Zimetti, C. Marchi, A. Bianchera, F. Bernini, M. Silvestri, R.
553 Bettini, L. Elviri, Study of 3D-printed chitosan scaffold features after different post-printing gelation
554 processes, Sci Rep. 9 (2019) 362. doi: 10.1038/s41598-018-36613-8.
555 [28] L. Elviri, R. Foresti, C. Bergonzi, F. Zimetti, C. Marchi, A. Bianchera, F. Bernini, M. Silvestri,
556 R. Bettini, Highly defined 3D printed chitosan scaffolds featuring improved cell growth, Biomed
557 Mater. 12 (2017) 045009. doi: 10.1088/1748-605X/aa7692.
558 [29] C. Intini, L. Elviri, J. Cabral, S. Mros, C. Bergonzi, A. Bianchera, L. Flammini, P. Govoni, E.
559 Barocelli, R. Bettini, M. McConnell, 3D-printed chitosan-based scaffolds: An *in vitro* study of human

skin cell growth and an *in-vivo* wound healing evaluation in experimental diabetes in rats. Carbohydrate polymers. 199 (2018) 593-602. doi: 10.1016/j.carbpol.2018.07.057.

[30] C. Manzoni, D.A. Kia, J. Vandrovcova, J. Hardy, N.W. Wood, P.A. Lewis, R. Ferrari, Genome, transcriptome and proteome: the rise of omics data and their integration in biomedical sciences, Briefings in Bioinformatics. 19 (2018) 286–302. https://doi.org/10.1093/bib/bbw114.

[31] A. Lovric, M. Granér, E. Bjornson, M. Arif, R. Benfeitas, K. Nyman, M. Ståhlman, M.O. Pentikäinen, J. Lundbom, A. Hakkarainen, R. Sirén, M.S. Nieminen, N. Lundbom, K. Lauerma, M.R. Taskinen, A. Mardinoglu, J. Boren, Characterization of different fat depots in NAFLD using inflammation-associated proteome, lipidome and metabolome, Scientific reports. 8 (2018) 14200. https://doi.org/10.1038/s41598-018-31865-w.

[32] A. Echard, D. Burgess, The Changing Lipidome during Cell Division, *Cell.* 156 (2014) 394-395. http://dx.doi.org/10.1016/j.cell.2014.01.018.

[33] Y.C. Kao, P.C. Ho, Y.K. Tu, I.M. Jou, K.J. Tsai, Lipids and Alzheimer's Disease, Int. J. Mol. Sci. 21 (2020) 1505. https://doi.org/10.3390/ijms21041505.

[34] D. Fontaine, S. Figiel, R. Felix, S. Kouba, G. Fromont, K. Mahéo, M. Potier-Cartereau, A. Chantome, C. Vandier, Roles of endogenous ether-lipids and associated PUFA in the regulation of ion channels and their relevance for disease, The Journal of Lipid Research. 61 (2020). doi: 10.1194/jlr.RA120000634.

[35] F. Mollinedo, C. Gajate, Lipid rafts as signaling hubs in cancer cell survival/death and invasion: implications in tumor progression and therapy, The Journal of Lipid Research. (2020). doi: 10.1194/jlr.TR119000439.

[36] A.C. Kendall, M.M. Koszyczarek, E.A. Jones, P.J. Hart, M. Towers, C. Griffiths, M. Morris, A. Nicolaou, Lipidomics for translational skin research: A primer for the uninitiated, Experimental Dermatology. 27 (2018) 721–728. https://doi.org/10.1111/exd.13558.

584 [37] H.C. Lee, T. Yokomizo, Applications of mass spectrometry-based targeted and non-targeted
585 lipidomics, Biochemical and Biophysical Research Communications. 504 (2018) 576–581.
586 https://doi.org/10.1016/j.bbrc.2018.03.081.
587 [38] M. Ohba, K. Saeki, T. Koga, T. Okuno, Y. Kobayashi, T. Yokomizoa, Profiling of bioactive
588 lipids in different dendritic cell subsets using an improved multiplex quantitative LC-MS/MS method,
589 Biochemical and Biophysical Research Communications. 504 (2018) 562-568.
590 https://doi.org/10.1016/j.bbrc.2018.06.026.
591 [39] C. Giles, R. Takechi, V. Lam, S. Dhaliwal, J. Mamo, Contemporary lipidomic analytics:
592 opportunities and pitfalls, Progress in Lipid Research. 71 (2018) 86-100.
593 https://doi.org/10.1016/j.plipres.2018.06.003.
594 [40] M.J. Choi, H.I. Maibach, Role of Ceramides in Barrier Function of Healthy and Diseased Skin,
595 Am J Clin Dermatol. 6 (2005) 215–223. https://doi.org/10.2165/00128071-200506040-00002.
596 [41] H. Alrbyawi, I. Poudel, R.P. Dash, N.R. Srinivas, A.K. Tiwari, R.D. Arnold, R. Jayachandra
597 Babu, Role of Ceramides in Drug Delivery, AAPS PharmSciTech. 20 (2019) 287.
598 https://doi.org/10.1208/s12249-019-1497-6.
599 [42] Z. Hu, S. Nizzero, S. Goel, E.L. Hinkle, X. Wu, C. Li, M. Ferrari, H. Shen, 2020. Molecular
600 targeting of FATP4 transporter for oral delivery of therapeutic peptide, Science Advances.
601 6(14),eaba0145. DOI: 10.1126/sciadv.aba0145.
602 [43] Y.C. Yung, N.C. Stoddard, J. Chun, LPA receptor signaling: pharmacology, physiology, and
603 pathophysiology, Journal of lipid research. 55 (2014) 1192–1214.
604 https://doi.org/10.1194/jlr.R046458.
605 [44] G. Tigyi, Aiming drug discovery at lysophosphatidic acid targets, British journal of
606 pharmacology. 161 (2010) 241–270. https://doi.org/10.1111/j.1476-5381.2010.00815.x.
607 [45] W. Drobnik, G. Liebisch, F.X. Audebert, D. Frohlich, T. Gluck, P. Vogel, G. Rothe. G. Schmitz,
608 Plasma ceramide and lysophosphatidylcholine inversely correlate with mortality in sepsis patients,
609 The Journal of Lipid Research. 44 (2003) 754-761. doi: 10.1194/jlr.M200401-JLR200.

[46] H.C. Tseng, C.C. Lin, L.D. Hsiao, C.M. Yang, Lysophosphatidylcholine-induced mitochondrial fission contributes to collagen production in human cardiac fibroblasts, The Journal of Lipid Research. 60 (2019) 1573-1589. doi: 10.1194/jlr.RA11900014.

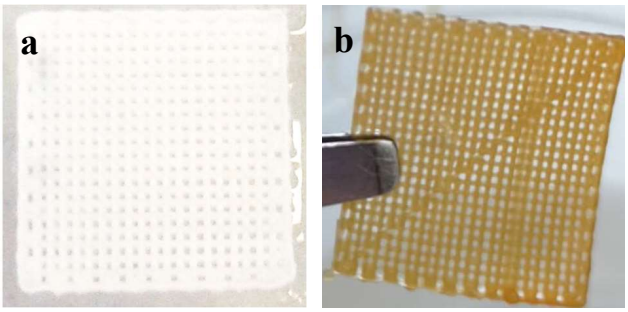

Figure 1. 3D printed alginate scaffolds gelled by: (a) $CaCl_2$ and (b) $FeCl_3$.

655
656
657
658
659
660
661
662
663
664
665
666
667
668
669
670
671
672
673
674
675
676
677
678
679
680
681
682
683
684
685
686
687
688

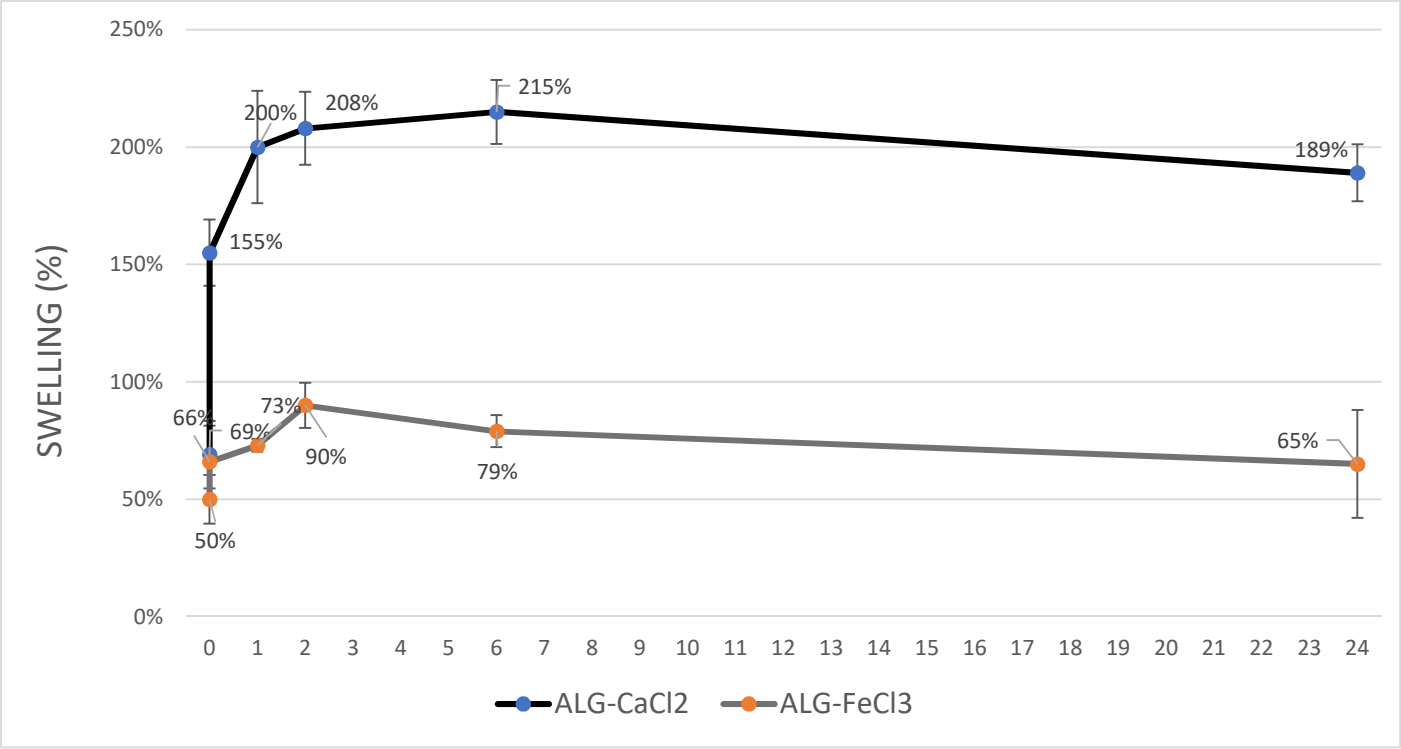

Figure 2. Swelling test of 3D_ALG_Ca (dark grey) and 3D_ALG_Fe (light grey) at different time point (n=5).

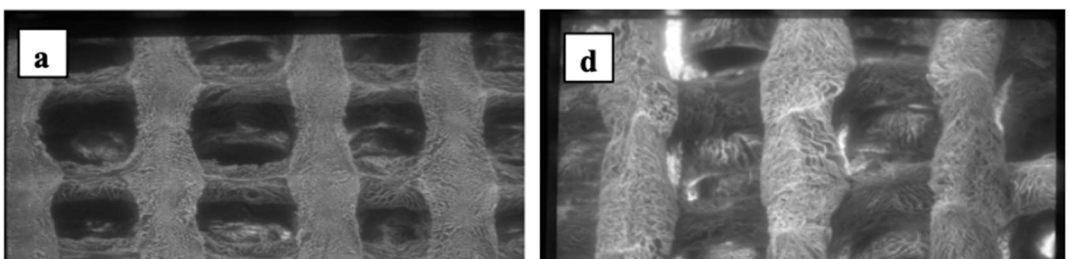

Figure 3. SEM image of 3D_ and 2D_ALG gelled with (a-c-g) $CaCl_2$ and (d-f-h) with $FeCl_3$ (4b). (a, b) 80X magnification; (b, e) 240X magnification; (c) 640X magnification; (f) 320X magnification; (g, h) 300X magnification.

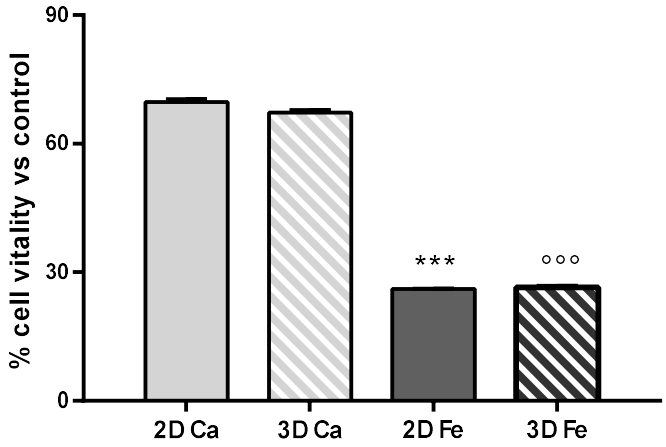

761

762 **Figure 4.** Cell vitality evaluated by MTT assay. ***p<0.001 vs 2D Ca; °°°p<0.001 vs 3D Ca.
763

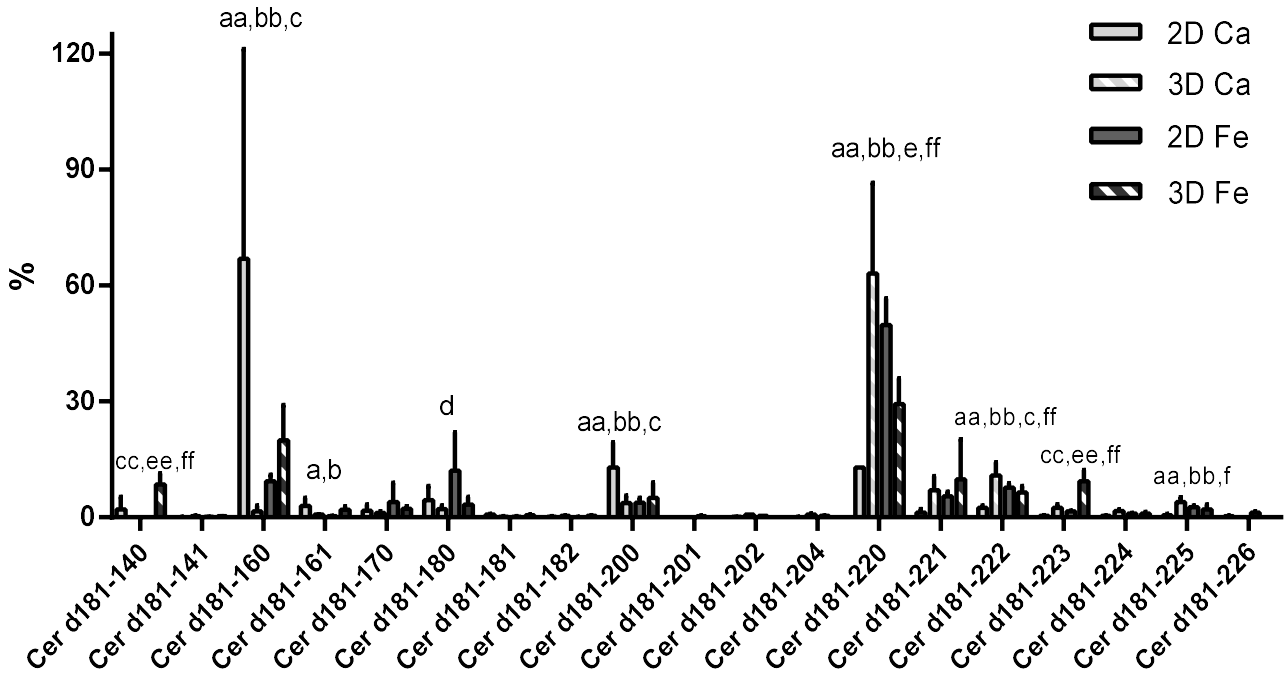

Figure 5. Percentage abundance of ceramides in human fibroblast cells grown on 2D_ and 3D_ALG_Ca or 2D_ and 3D_ALG_Fe . a: $p<0.05$ for 2D Ca vs 3D Ca, aa: $p<0.01$ for 2D Ca vs 3D Ca; b: $p<0.05$ for 2D Ca vs 2D Fe, bb: $p<0.01$ for 2D Ca vs 2D Fe; c: $p<0.05$ for 2D Ca vs 3D Fe, cc: $p<0.01$ for 2D Ca vs 3D Fe; d: $p<0.05$ for 2D Fe vs 3D Ca; e: $p<0.05$ for 2D Fe vs 3D Fe, ee: $p<0.01$ for 2D Fe vs 3D Fe; f: $p<0.05$ for 3D Fe vs 3D Ca, ff: $p<0.01$ for 3D Fe vs 3D Ca.

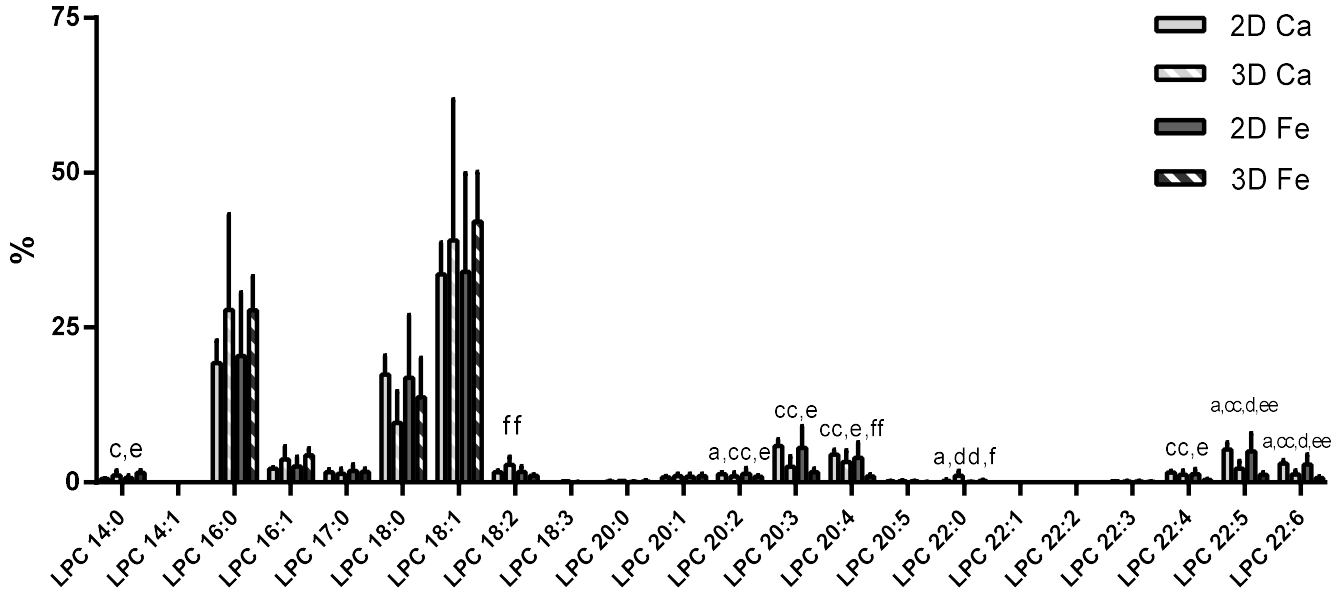

Figure 6. Percentage abundance of LPCs in human fibroblast cells grown on 2D_ and 3D_ALG_Ca or 2D_ and 3D_ALG_Fe. a: $p<0.05$ for 2D Ca vs 3D Ca; c: $p<0.05$ for 2D Ca vs 3D Fe, cc: $p<0.01$ for 2D Ca vs 3D Fe; d: $p<0.05$ for 2D Fe vs 3D Ca; dd: $p<0.01$ for 2D Fe vs 3D Ca; e: $p<0.05$ for 2D Fe vs 3D Fe, ee: $p<0.01$ for 2D Fe vs 3D Fe; f: $p<0.05$ for 3D Fe vs 3D Ca, ff: $p<0.01$ for 3D Fe vs 3D Ca.

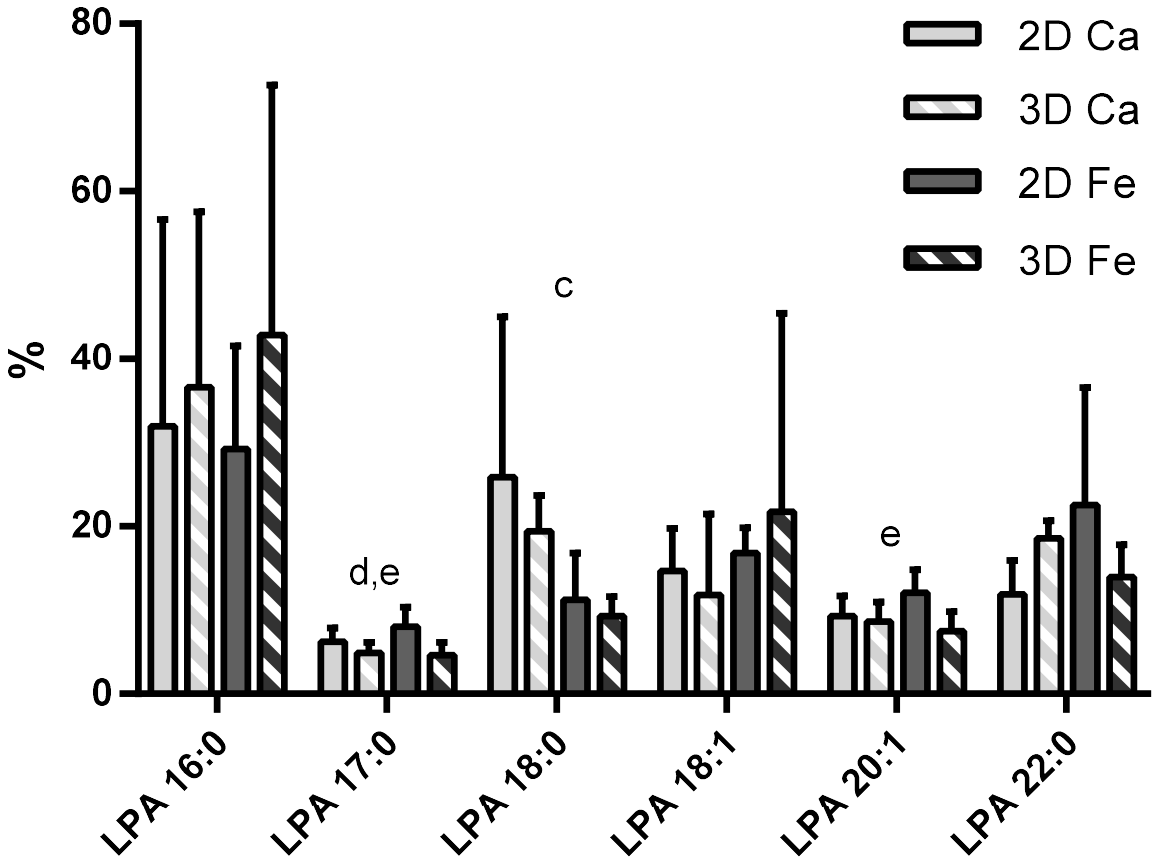

Figure 7. Percentage abundance of LPAs in human fibroblast cells grown on 2D_ and 3D_ALG_Ca or 2D_ and 3D_ALG_Fe. c: $p<0.05$ for 2D Ca vs 3D Fe; d: $p<0.05$ for 2D Fe vs 3D Ca; e: $p<0.05$ for 2D Fe vs 3D Fe.

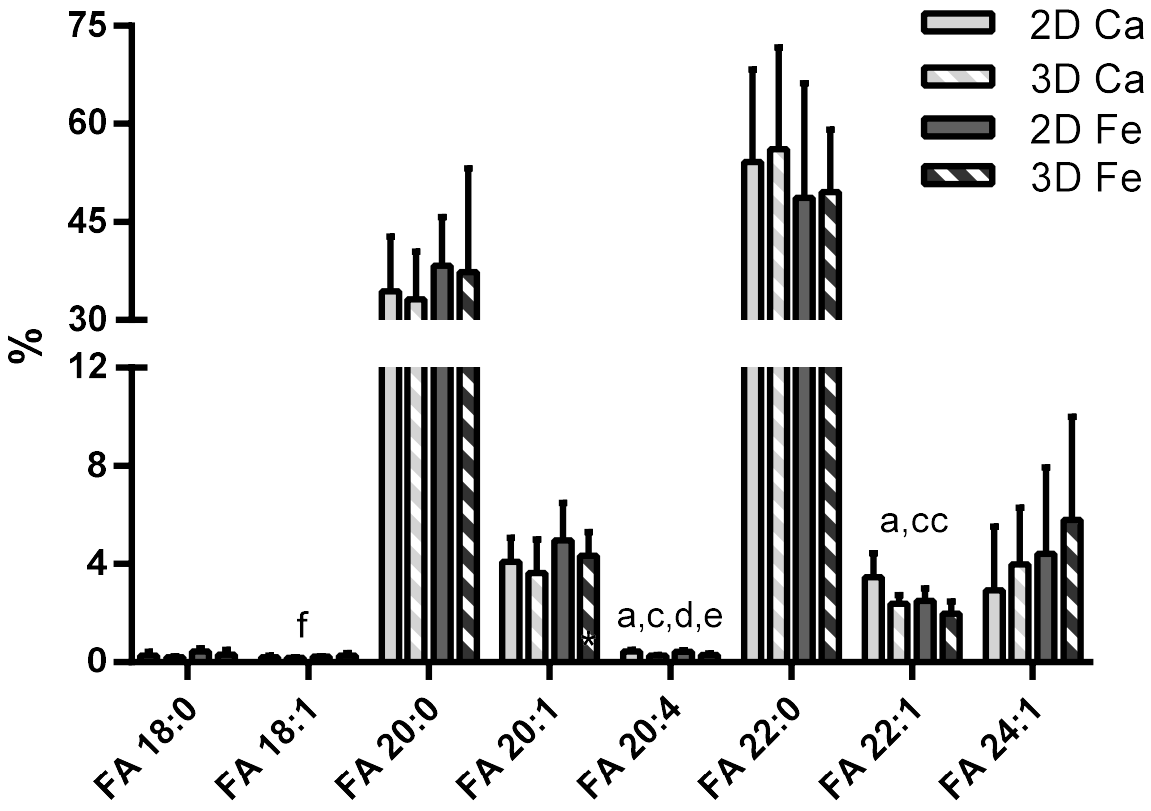

Figure 8. Percentage abundance of FFAs in human fibroblast cells grown on 2D_ and 3D_ALG_Ca or 2D_ and 3D_ALG_Fe. a: $p<0.05$ for 2D Ca vs 3D Ca; c: $p<0.05$ for 2D Ca vs 3D Fe, cc: $p<0.01$ for 2D Ca vs 3D Fe; d: $p<0.05$ for 2D Fe vs 3D Ca; e: $p<0.05$ for 2D Fe vs 3D Fe.